

# Patch-Depth Fusion: Dichotomous Image Segmentation via Fine-Grained Patch Strategy and Depth Integrity-Prior

Xianjie Liu

Sichuan university  
College of Computer Science  
liuxianjie.scu@vip.163.com

Keren Fu\*

Sichuan university  
College of Computer Science  
fkrsuper@scu.edu.cn

Qijun Zhao

Sichuan university  
College of Computer Science  
qjzhao@scu.edu.cn

## Abstract

*Dichotomous Image Segmentation (DIS) is a high-precision object segmentation task for high-resolution natural images. The current mainstream methods focus on the optimization of local details but overlook the fundamental challenge of modeling the integrity of objects. We have found that the depth integrity-prior implicit in the pseudo-depth maps generated by Depth Anything Model v2 and the local detail features of image patches can jointly address the above dilemmas. Based on the above findings, we have designed a novel Patch-Depth Fusion Network (PDFNet) for high-precision dichotomous image segmentation. The core of PDFNet consists of three aspects. Firstly, the object perception is enhanced through multi-modal input fusion. By utilizing the patch fine-grained strategy, coupled with patch selection and enhancement, the sensitivity to details is improved. Secondly, by leveraging the depth integrity-prior distributed in the depth maps, we propose an integrity-prior loss to enhance the uniformity of the segmentation results in the depth maps. Finally, we utilize the features of the shared encoder and, through a simple depth refinement decoder, improve the ability of the shared encoder to capture subtle depth-related information in the images. Experiments on the DIS-5K dataset show that PDFNet significantly outperforms state-of-the-art non-diffusion methods. Due to the incorporation of the depth integrity-prior, PDFNet achieves or even surpassing the performance of the latest diffusion-based methods while using less than 11% of the parameters of diffusion-based methods. The source code at [PDFNet](#).*

## 1. Introduction

With the continuous advancement of digital technology, obtaining high-precision images has become increasingly easier. The subsequent challenge is how to achieve high-precision segmentation from these high-resolution images.

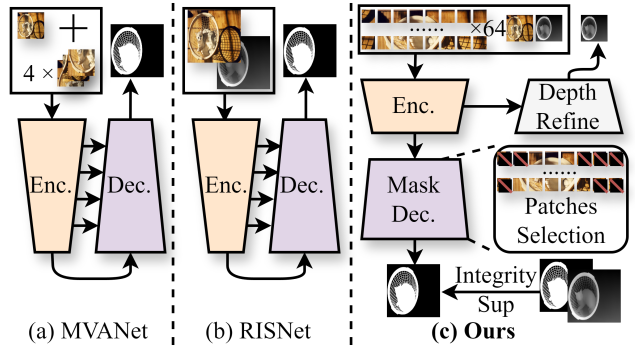


Figure 1. The comparison between our proposed PDFNet network and other existing methods for DIS tasks and RGB-D COD tasks. (a) MVANet: adopts 4 patches for multi-view input. (b) RISNet: employs dual-modal joint learning. (c) Ours: uses the patch fine-grained strategy, adopts the patch selection strategy, and utilizes the depth integrity-prior loss. Enc. = Encoder, Dec. = Decoder.

The DIS (Dichotomous Image Segmentation) task [1] focuses on segmenting high-precision objects from high-pixel images, meeting the growing demand for high-precision human-computer interaction across a wide range of applications. The primary goal of DIS is the accurate segmentation of fine-grained targets. However, due to occlusions, complex lighting conditions, and transparent glass, high-precision images contain numerous complex features that can easily lead to errors, making it difficult to isolate an object individually.

Recently, some well-known methods include MVANet [2] and DiffDIS [3]. The former introduced a multi-view aggregation method. It divides the image into multiple views to supplement local details, thus achieving the segmentation of complex details. The latter performs the DIS task by fine-tuning pre-trained diffusion models and adding an edge-generation task. Recently, some studies have found that the addition of pseudo-depth is helpful for dense prediction tasks. For example, Polyp-DAM [4] utilizes the pseudo-depth maps generated by DAM to enhance medical

image analysis through the perception of shape boundaries.

In this work, we introduce a method as Fig. 1. We observe that in high-precision images, depth integrity-prior helps in understanding objects as a whole, thereby reducing segmentation errors caused by local complex features. We found that depth images inherently contain rich and accurate **integrity-priors**: the depth distribution of segmented targets in the depth map is uniform and has few abrupt changes as Fig. 2. In addition, we have noticed that by inputting the image in patches [2, 5] and forcibly limiting the receptive field of the encoder for the image, can improve the sensitivity of the model to the details of the target. Therefore, our goal is to utilize the depth integrity-prior implicit in the pseudo-depth maps generated by Depth Anything Model (DAM) V2 [6] to compensate for the limitations of the model in understanding object integrity. Additionally, through the fine-grained patch strategy (from  $2 \times 2$  [2] or  $3 \times 3$  [5] to  $8 \times 8$ ), we aim to enhance the model’s ability to handle the details at the boundaries. To achieve this, we design a novel Patch-Depth Fusion Network (PDFNet), which cleverly combines the depth integrity-priors in the pseudo-depth map with local detail features in the patches. This design enhances the interaction between different types of information and facilitates the extension to more information modes. In addition, we proposed a depth integrity-prior loss to constrain the uniformity and continuity of the segmented target in the depth map.

Our main contributions can be summarized as follows:

- Innovatively introduce the depth integrity-prior through the pseudo-depth map, enabling the model to understand the object structure from a three-dimensional spatial perspective. Push the number of image patches to the extreme to enhance the model’s ability to handle the details.
- Elaborately design the PDFNet. PDFNet can skillfully fuse the depth integrity-prior in the pseudo-depth map and the prior of local details in patches, providing a new and effective solution for the binary image segmentation (DIS) task.
- Propose a novel feature selection mechanism and a depth integrity-prior loss. The former improves the incorrect extraction of non-target areas by the patch selection mechanism, and the latter enhances the uniformity and continuity of the results.
- PDFNet achieves the **state-of-the-art** among non-diffusion models in most metrics within the DIS-5K dataset. By complementing the depth integrity-prior, it can reach a performance level close to or even surpassing that of diffusion models while having fewer than 11% of the parameters of diffusion models.

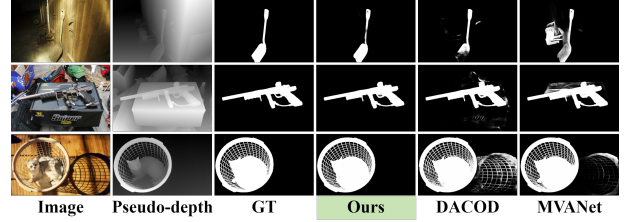


Figure 2. The Motivation of Depth Integrity-Prior. Given an image, the overall variance of the depth corresponding to its Ground Truth (GT) is small, and the depth changes are continuous. Inspired by this observation, we propose the integrity-prior loss. Compared with the recent RGB-D method DACOD [7] and DIS method MVANet [2], our results are closer to the ground truth.

## 2. Related works

### 2.1. Dichotomous Image Segmentation

Dichotomous image segmentation (DIS) is a segmentation task defined on the complex structures of natural images. Unlike traditional segmentation, it focuses on segmenting extremely fine-grained targets and the intricate internal structures of objects within natural images, making the segmentation particularly challenging.

Numerous efforts have been made to address DIS. The first notable work is IS-Net [1], which introduced the DIS5K dataset, utilized U2-Net [8] as the backbone network, and implemented an intermediate supervision strategy for DIS task. Additionally, FP-DIS [9] improved the accuracy of fine-grained object segmentation by leveraging frequency prior information. UDUN [10] proposed a dual-input strategy and a divide-and-conquer module to adapt to the DIS task. InSPyReNet [11] combines multi-scale feature extraction and refinement operations to achieve high-precision segmentation of complex images. BiRefNet [12] introduced a bilateral reference framework to enhance the precision of segmentation tasks. MVANet [2] proposed a multi-view aggregation method, segmenting complex details by dividing the image into multiple views to supplement local details. Genpercept [13] fine-tuning the diffusion models pre-trained on large-scale image-text pairs to enhance the precision of segmentation tasks. DiffDIS [3] introduces an auxiliary edge-generation task, which enhances the edge detection for the DIS task. However, all the above-mentioned methods overly rely on local features and lack the perception of 3D structures. They may mis-segment complex and occluded regions due to overlooking the overall shape of the object.

Different from these methods, we innovatively introduce pseudo-depth maps. By leveraging the depth integrity-prior implicit in the depth maps, we can constrain the overall rationality of the segmentation results. Meanwhile, by combining the local detail representation of image patches, we can achieve high-precision segmentation in complex scenes.

## 2.2. Monocular depth refinement

Monocular depth refinement predicts scene depth from single RGB images, forming the basis for pseudo-depth generation. Monodepth [14] was among the first to utilize an end-to-end deep learning model, achieving efficient monocular depth refinement by designing a disparity-based unsupervised loss function. Depth Anything Model (DAM) [15] further enhanced the accuracy and global consistency of monocular depth refinement by combining large-scale pre-training with a Transformer architecture. DAM v2 [6] replaces real annotated images with synthetic images, expanding the capacity of the teacher model. It then trains the student model using a large number of real images with pseudo-annotations, addressing the problem of insufficient accuracy in real-data annotation. DAM v2 achieves an accuracy rate of 97.1% on the DA-2K benchmark [6] and has become an important tool for pseudo-depth generation.

## 2.3. Real/Pseudo Depth Maps for Dense Prediction

Depth-aware methodologies in dense prediction have evolved through two complementary paradigms: real-depth sensing for hardware-enabled scenarios and pseudo-depth generation for RGB-only settings.

Real-Depth Approaches demonstrate the value of geometric perception in RGB-D tasks but face hardware constraints. For salient object detection, MAGNet [16] employs dual-stream encoding while CPNet [17] introduces cross-modal attention fusion. In camouflaged detection, DACOD [7] proposes asymmetric fusion strategies whereas RISNet [18] enhances multi-scale learning. These methods share a common philosophy of fusing depth-induced 3D cues with RGB textures, yet remain limited by their dependency on specialized sensors.

Pseudo-Depth Paradigms overcome hardware barriers through synthetic depth generation. [19] introduces pseudo-depth maps and enhances the performance of instance segmentation by constraining depth consistency. [20] shows pseudo-depth maps enable unknown category segmentation. Polyp-DAM [4] utilizes the pseudo-depth maps generated by DAM to enhance medical image analysis through the perception of shape boundaries. [21] uses the pseudo-depth maps generated by DAM v2, which improves the model’s perception of the target shape and boundaries and enhances the counting accuracy. Essentially, these pseudo-depth maps address the structural deficiencies in 2D models through pseudo-3D representation methods.

Our work synthesizes these insights by transplanting the depth-aware integrity-prior knowledge into the DIS through pseudo-depth mapping. We have also designed task-specific fusion modules and loss function. While enforcing three-dimensional structural constraints, these modules and loss function preserve the precision.

## 3. Method

In this section, we present the approach in detail, including the overall architecture and specific components.

### 3.1. Overall Architecture

**Pseudo-depth map generation.** DAM v2, through training with ultra-large-scale synthetic data and using a large amount of real-world data with pseudo-labels to teach the student model, can generate highly accurate pseudo-depth maps. The HR input images  $I \in \mathbb{R}^{B \times 3 \times H \times W}$  are fed into DAM v2, and the normalized relative monocular depth refinement maps  $D \in \mathbb{R}^{B \times 1 \times H \times W}$  with values ranging from 0 to 1 are obtained as the pseudo-depth maps. This pseudo-depth map will be input into PDFNet as a feature representing the depth integrity-prior.

**Multi-stage Feature Extraction.** Based on the shared encoder framework [2, 5, 22], this paper constructs a cross-modal feature interaction system. For a high-resolution RGB image  $I \in \mathbb{R}^{B \times 3 \times H \times W}$  and a depth map  $D \in \mathbb{R}^{B \times 1 \times H \times W}$ , after performing a  $1/2$  down-sampling operation respectively, the feature sequences  $\{F_i^v\}_{i=1}^4$  and  $\{F_i^d\}_{i=1}^4$  are generated. To enhance the detail representation, the original image is reorganized into  $\mathbb{R}^{64 \times B \times 3 \times \frac{H}{8} \times \frac{W}{8}}$  after being divided into 64 patches [2, 5]. The patch encoder is used to extract the features  $\{F_i^{pj}\}_{j=0}^{63}$ , and after spatial reorganization, the sequence  $\{F_i^p\}_{i=1}^4$  with a resolution twice that of the visual/depth features is formed. In the feature aggregation stage, cross-scale  $3 \times 3$  convolutions are used for fusion to generate  $\{F_5^v, F_5^d, F_5^p\}$ , where  $\{F_i^v, F_i^d\}$  are responsible for spatial positioning, and  $\{F_i^p\}$  is specifically for detail representation. This architecture achieves modal complementarity through hierarchical feature interaction and improves feature consistency.

**Refinement Decoding.** Our network is different from the classic U-net. As shown in the Fig. 3, we insert a feature selection and extraction (FSE) module at each stage. These modules can selectively enhance the corresponding features according to the prediction results of the previous stage of the network using prediction boundary-integrity separation. At the same time, these modules can gradually fuse multi-modal information through multi-modal cross-attention. Finally, the shallow features will also be absorbed layer by layer into the upsampling path of the decoder to achieve context-complementary fusion.

**Depth Refinement.** By introducing the depth refinement task, adding a pseudo-depth prediction branch is equivalent to introducing a regularization constraint for the encoder, forcing the extracted features to meet the requirements of both the segmentation task and the depth refinement task simultaneously. We introduce the features obtained by adding up the three modalities into a new lightweight depth decoder to predict the highest-quality pseudo-depth refinement la-

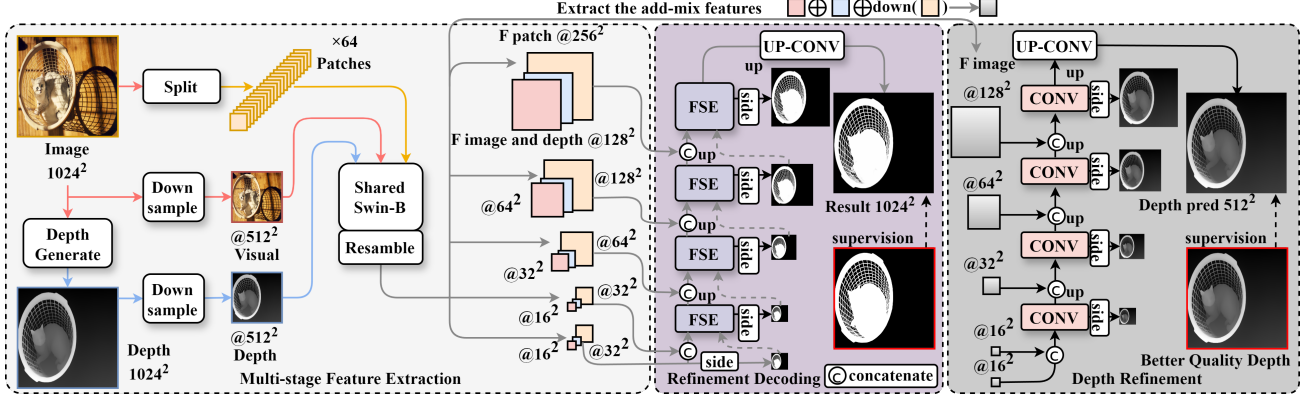


Figure 3. Overall pipeline of our proposed PDFNet.

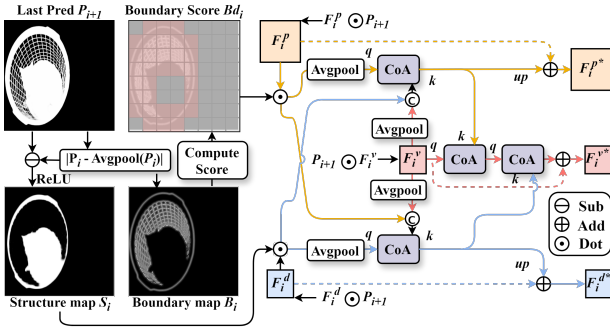


Figure 4. Feature selection and extraction (FSE) module.

bels generated by DAM v2-large [6]. We simply process the input features by concatenating two Conv 3×3 silu and RMSNorm blocks at each stage of the decoder. Then, the processed features are output through a Conv 3×3 head.

**Multi-feature merging supervision.** Deep supervision has been proven effective for the DIS task in many studies as [1, 2, 10, 12]. As shown on the Fig. 3, we conduct intermediate supervision on the target results. After all the above steps, we will obtain  $P \in \mathbb{R}^{B \times 3 \times \frac{H}{4} \times \frac{W}{4}}$ , whose shape is one quarter of that of the target. Finally, through two successive upsampling operations, we incorporate the shallow features [2, 23] of vision and depth as low-level visual cues, so as to further improve the quality of image segmentation. We also perform similar operations on the depth refinement decoder and conduct multi-stage supervision.

### 3.2. Feature Selection and Extraction (FSE)

The patches approach enhances the ability to extract details by limiting the receptive field of the encoder on the image. However, this may cause it to focus too much on detail extraction and break its connection with the context. To ensure that the features extracted by patches are the edge features required for the segmentation target, we designed the FSE module. It dynamically selects patches based on the prediction output of the previous layer, forming a de-

tailed feature representation that is sensitive to the target boundaries and suppresses non-target boundaries. The attention mechanism enables hierarchical interaction between global and local features, enhancing the feature discrimination ability in complex scenarios. The process of the FSE module is divided into two stages.

First, based on the prediction result  $P_{i+1}$  from the previous stage, a boundary-integrity separation strategy is adopted to generate a boundary response map and an internal region integrity map. Given that the size of  $P_{i+1} \in \mathbb{R}^{B \times 1 \times H \times W}$ , an average pooling operation is performed on  $D_{i+1}$  to obtain  $P_{p_{i+1}}$ . The absolute difference between  $P_{i+1}$  and  $P_{p_{i+1}}$  is calculated and multiplied by a coefficient of 2 to amplify the response, resulting in the boundary response map  $B_i$ . This process enhances the gradient change in the edge region. Mathematically, we can represent these operations as follows:

$$P_{p_{i+1}} = \text{AvgPool}(P_{i+1}), \quad (1)$$

$$B_i = 2 \cdot |P_{i+1} - P_{p_{i+1}}|. \quad (2)$$

Finally, the original prediction result  $P_{i+1}$  is subtracted by five times the boundary response  $B_i$  and then processed through ReLU thresholding to obtain the target integrity map  $S_i$  after boundary suppression, which focuses on the feature representation of the continuous regions inside the target.

$$S_i = \text{ReLU}(P_{i+1} - \lambda_B \cdot B_i), \quad (3)$$

where the kernel size of the average pooling is  $(H/8, W/8)$  to adapt to inputs of different resolutions, which reduces the image resolution by half, and  $\lambda_B$  is set to 5. The strategy uses a difference amplification mechanism to enhance boundary sensitivity and maintains the consistency of the internal structure through nonlinear suppression. The finally obtained boundary response map  $B_i$  is divided into 64 patches corresponding to the number of patches. After global average pooling, the boundary response score  $Bd_i$  for each patch is obtained. A weighting mechanism is used



to assign corresponding weights to each patch, suppressing the redundant details in non-target edge regions and forming a detailed feature representation that is sensitive to the target boundaries.

Second, to enable effective multi-modal fusion, we propose the Cross-modal Attention (CoA) module. Leveraging cross-attention mechanisms, CoA dynamically allocates inter-modal weights through query-key-value interactions, where complementary information is selectively enhanced via Q/K projections. The process involves: (1) Attention [24] computation  $\text{Att}(Q, K)$  between pixel sequences, (2) Integration of original Q with RMSNorm-normalized [25] attention output, (3) Non-linear enhancement through  $\text{FFN}_{\text{SwiGLU}}$  [26] with residual connections to produce final representation  $F$ . For GPU memory efficiency, we design hierarchical feature processing: Original features  $F_i^v, F_i^d, F_i^p$  are element-wise multiplied with  $P_{i+1}$ , then compressed via stage-specific average pooling to obtain  $FP_i^c, FP_i^d, FP_i^p$  [2, 27, 28]. These are tokenized and concatenated into cross-modal composites  $FP_i^{vd}$  (visual-depth) and  $FP_i^{vp}$  (visual-pose), enabling continuous inter-modal interaction. Image serialization is applied before CoA computation for attention optimization. Then, cross-modal feature associations are established through CoA, and the structural constraints of depth features and local detail features are dynamically integrated into the global context through  $F_i^v$ :

$$FN_i^{p*} = \text{CoA}(FP_i^p \odot (1 + \lambda_{bd} \cdot Bd_i), FP_i^{vd}), \quad (4)$$

$$FN_i^{d*} = \text{CoA}(FP_i^d \odot (P_{i+1} + S_i), FP_i^{vp}), \quad (5)$$

$$FN_i^{v1*} = \text{CoA}(F_i^{v*}, FN_i^{p*}), \quad (6)$$

$$FN_i^{v2*} = \text{CoA}(FN_i^{v1*}, FN_i^{d*}). \quad (7)$$

where the  $\lambda_{bd}$  is set to 5. Finally the visual, patches and depth are updated through residual links:

$$F_i^{v*} = F_i^v + FN_i^{v2*}, \quad (8)$$

$$F_i^{p*} = F_i^p + \text{up}(FN_i^{p*}), \quad (9)$$

$$F_i^{d*} = F_i^d + \text{up}(FN_i^{d*}). \quad (10)$$

### 3.3. Integrity-Prior Loss

We have noticed that the values of the segmentation targets in the depth map are generally relatively uniform. We refer to this as the integrity-prior. To maintain this integrity-prior, we suppress abnormal gradient responses while preserving the internal continuity of the target region in two ways. Different from [19], which calculates adjacent depth values pixel by pixel to limit the overall depth consistency, we maintain the depth integrity-prior through the mean and gradient. First is the depth stability constraint. Based on the statistical characteristics of the depth value distribution within the mask region, we aim to reduce the phenomena where, in the  $\mathcal{FP}$  (False Positive) region, the depth values

significantly differ from the mean depth of the target but are incorrectly predicted, and in the  $\mathcal{FN}$  (False Negative) region, the depth values are similar to the mean of the target region but are missed. Specifically, the loss of the target segmentation in the corresponding region is required to be weighted according to the differences in its depth values, so that the overall change in the corresponding depth values of the segmentation target is relatively small. Specifically, the average depth of the mask region is calculated first:

$$\mu = \frac{\sum(D \odot M)}{\sum M}. \quad (11)$$

Subsequently, calculate the differences between the depth means of the  $\mathcal{FP}$  and  $\mathcal{FN}$  regions and the depth mean of the ground truth region respectively, and assign weights based on these differences:

$$l_v = \mathbb{E}[-\log \mathcal{P}_y \odot (\text{diff} \odot (\mathcal{FP} - \mathcal{FN}) + \mathcal{FN})], \quad (12)$$

where  $D$  is the depth map,  $M$  is the binary ground truth,  $\epsilon$  is a coefficient for numerical stability and  $\mathcal{P}_y$ ,  $\text{diff}$ ,  $\mathcal{FP}$  and  $\mathcal{FN}$  are formulated as:

$$\mathcal{P}_y = P \odot M + (1 - P) \odot (1 - M), \quad (13)$$

$$\text{diff} = (D - \mu)^2, \quad (14)$$

$$\mathcal{FP} = (1 - \mathcal{P}_y) \odot P, \quad (15)$$

$$\mathcal{FN} = (1 - \mathcal{P}_y) \odot M. \quad (16)$$

Then is the depth continuity constraint. Based on the boundary distribution characteristics of the mask region, the Sobel operator is used to extract the horizontal and vertical gradients of the depth map. The corresponding depth continuity is controlled through the gradient amplitude statistics to reduce the spatial discontinuity of the depth map corresponding to the segmentation result:

$$l_g = \mathbb{E}[-\log \mathcal{P}_y \odot (|G_x| + |G_y|)], \quad (17)$$

where  $G_x$  and  $G_y$  are the horizontal/vertical gradient maps of the depth map obtained by the Sobel operator respectively. Through these two depth constraints, the model can utilize depth cues during the training process, which helps it distinguish between the interior and the boundary of the object, thereby achieving more accurate segmentation. Finally, the integrity-prior loss  $l_{inte}$  can be written in the following form:

$$l_{inte} = l_v + l_g. \quad (18)$$

### 3.4. Loss Function

We supervise the output of each layer in the decoder as well as the final prediction result. In addition, we also supervise the result of each layer in the depth refinement decoder. The supervision for the output of each layer is denoted as  $l_f^i$ , and the supervision for the final result is denoted as  $l_f$ . For the supervision of segmentation, following

Methods	Params	DIS-VD (470)					DIS-TE1 (500)					DIS-TE2 (500)				
		$F_{\beta}^{max}$	$\uparrow F_{\beta}^w$	$\uparrow E_{\phi}^m$	$\uparrow S_{\alpha}$	$\downarrow MAE$	$F_{\beta}^{max}$	$\uparrow F_{\beta}^w$	$\uparrow E_{\phi}^m$	$\uparrow S_{\alpha}$	$\downarrow MAE$	$F_{\beta}^{max}$	$\uparrow F_{\beta}^w$	$\uparrow E_{\phi}^m$	$\uparrow S_{\alpha}$	$\downarrow MAE$
MAGNet <sub>24</sub> [16]	16M	0.867	0.820	0.917	0.879	0.045	0.838	0.790	0.899	0.862	0.044	0.876	0.833	0.923	0.886	0.041
CPNet <sub>24</sub> [17]	216M	0.892	0.855	0.933	0.900	0.034	0.862	0.819	0.910	0.880	0.037	0.892	0.855	0.929	0.899	0.036
DACOD <sub>23</sub> [7]	189M	0.881	0.831	0.925	0.887	0.041	0.852	0.800	0.906	0.870	0.038	0.884	0.839	0.925	0.891	0.039
RISNet <sub>24</sub> [18]	25M	0.853	0.810	0.913	0.869	0.046	0.824	0.776	0.890	0.859	0.044	0.869	0.828	0.918	0.880	0.044
IS-Net <sub>22</sub> [1]	44M	0.791	0.717	0.856	0.813	0.074	0.740	0.662	0.820	0.787	0.074	0.799	0.728	0.858	0.823	0.070
FP-DIS <sub>23</sub> [9]	-	0.823	0.763	0.891	0.843	0.062	0.784	0.713	0.860	0.821	0.060	0.827	0.767	0.893	0.845	0.059
UDUN <sub>23</sub> [10]	25M	0.823	0.763	0.891	0.843	0.062	0.784	0.720	0.864	0.817	0.059	0.829	0.768	0.886	0.843	0.058
InSPyReNet <sub>22</sub> [11]	87.5M	0.889	0.834	0.914	0.900	0.042	0.845	0.788	0.894	0.873	0.043	0.894	0.846	0.916	0.905	0.036
BiRefNet <sub>24</sub> [12]	215M	0.897	0.854	0.931	0.898	0.038	0.866	0.819	0.911	0.885	0.037	0.906	0.857	0.930	0.900	0.036
MVNet <sub>24</sub> [2]	93M	0.904	0.856	0.938	0.905	0.036	0.873	0.823	0.911	0.879	0.037	0.916	0.874	0.944	0.915	0.030
GenPercept <sub>25</sub> [13]	865M+	0.877	0.859	0.941	0.887	0.035	0.850	0.827	0.919	0.878	0.036	0.880	0.859	0.938	0.892	0.034
DiffDIS <sub>25</sub> [3]	865M+	0.908	0.888	0.948	0.904	0.029	0.883	0.862	0.933	0.891	0.030	0.917	0.895	0.951	0.913	0.026
<b>PDFNet</b>	<b>94M</b>	<b>0.913</b>	<b>0.873</b>	<b>0.944</b>	<b>0.916</b>	<b>0.030</b>	<b>0.890</b>	<b>0.846</b>	<b>0.927</b>	<b>0.899</b>	<b>0.031</b>	<b>0.921</b>	<b>0.885</b>	<b>0.947</b>	<b>0.924</b>	<b>0.028</b>
Methods	Params	DIS-TE3 (500)					DIS-TE4 (500)					DIS-TE (ALL) (2,000)				
		$F_{\beta}^{max}$	$\uparrow F_{\beta}^w$	$\uparrow E_{\phi}^m$	$\uparrow S_{\alpha}$	$\downarrow MAE$	$F_{\beta}^{max}$	$\uparrow F_{\beta}^w$	$\uparrow E_{\phi}^m$	$\uparrow S_{\alpha}$	$\downarrow MAE$	$F_{\beta}^{max}$	$\uparrow F_{\beta}^w$	$\uparrow E_{\phi}^m$	$\uparrow S_{\alpha}$	$\downarrow MAE$
MAGNet <sub>24</sub> [16]	16M	0.893	0.850	0.935	0.893	0.039	0.870	0.820	0.923	0.870	0.049	0.869	0.823	0.920	0.878	0.043
CPNet <sub>24</sub> [17]	216M	0.922	0.887	0.950	0.916	0.028	0.895	0.856	0.935	0.896	0.039	0.893	0.854	0.931	0.898	0.035
DACOD <sub>23</sub> [7]	189M	0.904	0.855	0.938	0.901	0.037	0.869	0.812	0.915	0.873	0.053	0.878	0.827	0.921	0.884	0.042
RISNet <sub>24</sub> [18]	25M	0.889	0.852	0.936	0.888	0.038	0.865	0.826	0.929	0.866	0.048	0.862	0.820	0.918	0.873	0.044
IS-Net <sub>22</sub> [1]	44M	0.830	0.758	0.883	0.836	0.064	0.827	0.753	0.870	0.830	0.072	0.799	0.725	0.858	0.819	0.070
FP-DIS <sub>23</sub> [9]	-	0.868	0.811	0.922	0.871	0.049	0.846	0.788	0.906	0.852	0.061	0.831	0.770	0.895	0.847	0.057
UDUN <sub>23</sub> [10]	25M	0.865	0.809	0.917	0.865	0.050	0.846	0.792	0.901	0.849	0.059	0.831	0.772	0.892	0.844	0.057
InSPyReNet <sub>22</sub> [11]	87.5M	0.919	0.871	0.940	0.918	0.034	0.905	0.848	0.936	0.905	0.042	0.891	0.838	0.922	0.900	0.039
BiRefNet <sub>24</sub> [12]	215M	0.920	0.893	0.955	0.919	0.028	0.906	0.864	0.939	0.900	0.039	0.900	0.858	0.934	0.901	0.035
MVNet <sub>24</sub> [2]	93M	0.929	0.890	0.954	0.920	0.031	<b>0.912</b>	<b>0.857</b>	<b>0.944</b>	0.903	0.041	0.908	0.861	0.938	0.904	0.035
GenPercept <sub>25</sub> [13]	865M+	0.898	0.879	0.954	0.896	0.032	0.874	0.858	0.947	0.874	0.041	0.875	0.856	0.939	0.885	0.036
DiffDIS <sub>25</sub> [3]	865M+	0.934	0.916	0.964	0.919	0.025	0.909	0.893	0.955	0.896	0.025	0.911	0.892	0.951	0.905	0.027
<b>PDFNet</b>	<b>94M</b>	<b>0.936</b>	<b>0.900</b>	<b>0.957</b>	<b>0.928</b>	<b>0.027</b>	<b>0.911</b>	<b>0.867</b>	<b>0.941</b>	<b>0.910</b>	<b>0.037</b>	<b>0.915</b>	<b>0.874</b>	<b>0.943</b>	<b>0.915</b>	<b>0.031</b>

Table 1. Performance comparisons of PDFNet with MAGNet, CPNet, DACOD, RISNet, IS-Net, FP-DIS, UDUN, InSPyReNet, BiRefNet, MVNet, GenPercept and DiffDIS. The symbols  $\uparrow/\downarrow$  indicate that higher/lower scores are better. The best score is highlighted in **bold**, and the second is underlined without diffusion-based models because of the much larger parameters.

the practice of most segmentation tasks, we adopt a combination of weighted Binary Cross-Entropy [29] (wBCE), weighted Intersection over Union [29] (wIoU), and SSIM loss [30], following the practice of most segmentation tasks [1, 2, 12], and the integrity-prior loss proposed by us:

$$l = l_{wBCE} + l_{wIoU} + \frac{l_{SSIM}}{2} + \frac{l_{inte}}{2}. \quad (19)$$

For the supervision of depth refinement, we use the Scale Invariant Logarithmic error [31] (SILog) loss which is adopted in most tasks. Finally, our overall loss can be written in the following form:

$$L = l_f + \lambda_1 \cdot \sum_{i=1}^5 l^i + \lambda_2 \cdot l_{SILog} + \lambda_3 \cdot \sum_{i=1}^4 l_{SILog}^i, \quad (20)$$

where the  $\lambda_1$ ,  $\lambda_2$  and  $\lambda_3$  is set to 0.5, 0.1 and 0.05.

## 4. Experiment

### 4.1. Datasets and Evaluation Metrics

**Data Setup.** We conducted extensive experiments on DIS-5K [1]. DIS-5K consists of 5,470 images and 225 categories in total. It contains 6 subsets, namely DIS-TR, DIS-VD, DIS-TE(1-4). Among them, DIS-TR and DIS-VD are composed of 3,000 and 470 samples respectively. DIS-TE(1-4) are in the order from simple to complex, and each TE contains 500 samples.

**Pseudo-depth Map Generation.** We employ DAM v2 ([6]) to generate pseudo-depth maps. Three sizes (small, base, large) of DAM v2 are used to produce different qualities maps. With DAM v2's default settings, input images are resized to  $518^2$  and outputs to  $1024^2$ . Additionally, we utilize the  $1024^2$  input-output pseudo-depth map as the top-quality depth map for supervising depth refinement and  $l_{inte}$  losses. During testing, unless otherwise specified, only the pseudo-depth maps of large quality are used for testing.

**Testing Metrics.** To test the results, we select widely-

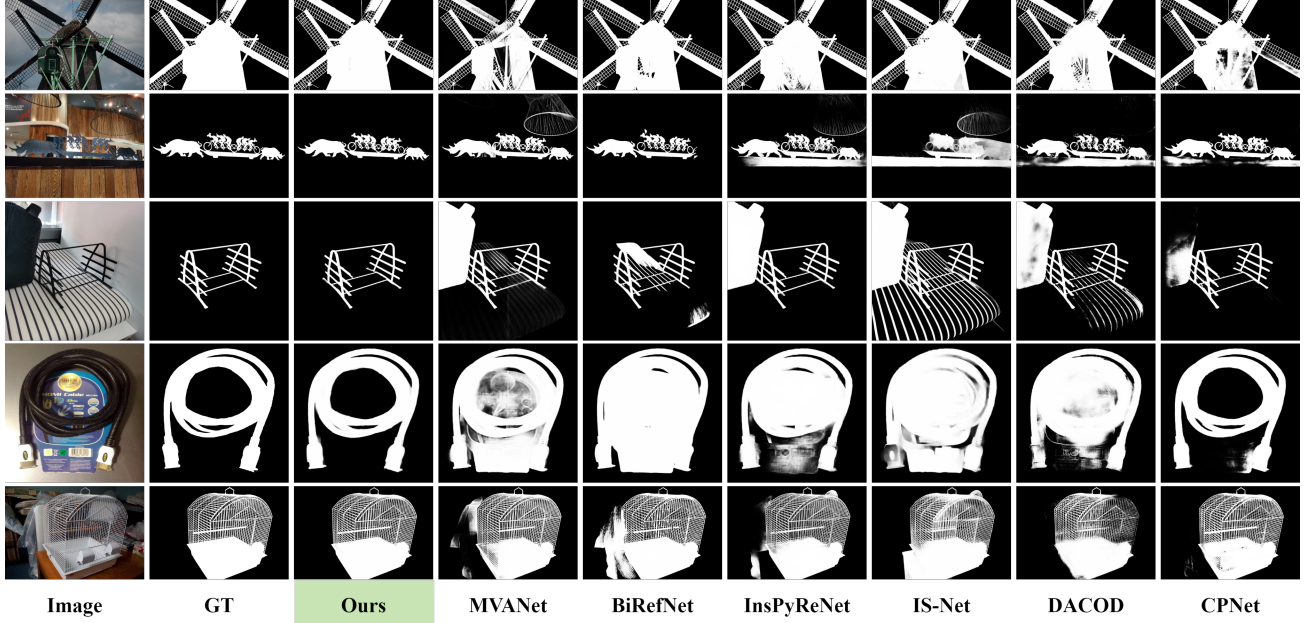


Figure 5. Visual comparison of different DIS and RGB-D SOC/COD methods.

used metrics same as [2, 3], including max F-measure [32] ( $F_{\beta}^{max}$ ), weighted F-measure [33] ( $F_{\beta}^w$ ), structural similarity measure [34] ( $S_{\alpha}$ ), E-measure [35, 36] ( $E_{\phi}^m$ ), and mean absolute error [37] ( $MAE$ ).  $F_{\beta}^{max}$  and  $F_{\beta}^w$  are the minimum values and weighted scores of precision and recall respectively, where  $\beta$  is set to 0.3.  $S_m$  simultaneously evaluates the region-aware and object-aware structural similarity between the prediction and the mask.  $E_{\phi}^m$  is widely used to evaluate pixel-level and image-level matching.  $MAE$  measures the average error of the prediction map.

## 4.2. implementation Details

The experiments were all deployed on a RTX-4090 using the PyTorch framework. During the training process, the input images were first resized to  $1024^2$ . Swin-B [38], which was pre-trained on ImageNet [39], was used as the backbone of the network. To avoid overfitting, we added some data augmentation methods, including random horizontal flipping, rotation, random color augmentation, and random cropping. We employed the AdamW optimizer with an initial learning rate of  $1 \times 10^{-5}$ . The batch size was set to 1, and the training ran for 100 epochs.

## 4.3. Comparison with State-of-the-arts

**Quantitative Evaluation.** In Table 1, we compare our PDFNet with other well-known task-related models. These models include CNN-based models such as IS-Net [1], FP-DIS [9], UDUN [10] and InSPyReNet [11], Transformer-based models like BiRefNet [12] and MVANet [2], and diffusion-based models GenPercept [13] and DiffDIS [3].

In addition, we also compare with the recent RGB-D SOD methods such as MAGNet [16] and CPNet [17], and RGB-D COD methods including DACOD [7] and RISNet [18] after they are trained on the DIS task. Except for the now non-open-source FP-DIS and DiffDIS, we adjust the input of all the other comparison models to  $1024^2$  for a fair comparison, while for FP-DIS and DiffDIS, we use the metrics presented in their papers. It can be seen that the metrics of PDFNet far exceed those of all the other non-diffusion models. For the best non-diffusion model MVANet, we exceed it by 0.9%, 1.3%, 0.5%, 1.1%, 0.4% in  $F_{\beta}^{max}$ ,  $F_{\beta}^w$ ,  $S_{\alpha}$ ,  $E_{\phi}^m$ ,  $MAE$  respectively on DIS-TE (ALL). Notably, in certain metrics, our model not only matches but far surpasses diffusion-based models. Moreover, the parameter count of our model is less than 11% of them.

**Qualitative Evaluation.** As shown in the Fig. 5, due to the incorporation of the depth integrity-prior, our model can locate the target more accurately in complex scenes. For example, in the images of the third row, without the guidance of the depth integrity-prior, other methods will overfit the details and mistakenly segment the patterns on the sofa. In contrast, our model can accurately segment the shelf.

## 4.4. Ablation Study

In this section, we analyzed the impact of pseudo-depth map quality and the influence of each module on the outcomes. All of them were tested only on DIS-VD.

Depth quality	$F_{\beta}^{max} \uparrow$	$F_{\beta}^w \uparrow$	$E_{\phi}^m \uparrow$	$S_{\alpha} \uparrow$	$MAE \downarrow$
PDFNet-s	0.909	0.868	0.942	0.913	<b>0.030</b>
PDFNet-b	0.912	<b>0.873</b>	<b>0.944</b>	<b>0.916</b>	<b>0.030</b>
PDFNet-l	<b>0.913</b>	<b>0.873</b>	<b>0.944</b>	<b>0.916</b>	<b>0.030</b>

Table 2. The influence of different qualities depth maps on the results during the testing.

FSE	Depth	$F_{\beta}^{max} \uparrow$	$E_{\phi}^m \uparrow$	$S_{\alpha} \uparrow$	$MAE \downarrow$	$FPS \uparrow$
		0.880	0.911	0.900	0.042	<b>7.300</b>
	✓	0.902	0.931	0.907	0.036	4.525
✓		0.903	0.937	0.907	0.036	6.043
✓	✓	<b>0.907</b>	<b>0.940</b>	<b>0.912</b>	<b>0.032</b>	3.925

Table 3. Ablation experiments of components.

#### 4.4.1 Pseudo-depth Map Quality

During training, we used pseudo-depth maps of random qualities. In the ablation, we tested different-quality pseudo-depth maps. PDFNet-s uses small-quality ones, and others follow suit. As Table 2 shows, better-quality pseudo-depth maps yield better results. When a depth map is available, PDFNet’s single-inference takes 165 ms. Without a depth map, we must consider the pseudo-depth map’s inference time and the model size. DAM v2-small (24M) needs 47 ms for one-time inference, the base (97M) takes 91 ms, and the large (335M) requires 127 ms. These times are significantly lower than those of the latest diffusion-based models, whose parameters exceed 865M.

#### 4.4.2 Components of PDFNet

**Baseline.** We provided a simple encoder-decoder architecture as the baseline, using  $8 \times 8$  patches. For the model with the FSE removed, we directly pass the results obtained from the encoder through a Conv3 $\times$ 3 layer, SiLU [40], and RMSNorm to adjust channel numbers and input them into the decoder of the next stage. For the model with the Depth removed, we set the depth input to all zeros and do not calculate the time taken for generating the pseudo-depth maps. For the entire ablation of components, we did not use  $L_{SILog}$  and  $L_{inte}$ . **FSE.** As shown in the Table 3, the Feature Selection and Fusion Encoder (FSE) plays the roles of selecting patches and fusing modalities. Compared with adding only depth, adding the FSE module can enhance the degree of modal fusion and thus improve  $F_{\beta}^{max}$ . **Depth.** Pseudo-depth plays a crucial role in providing the integrity-prior throughout the process, significantly enhancing the ability to detect the integrity of the target.

#### 4.4.3 Depth Loss

As shown in the Table 4, each element has a positive impact on the performance. It is worth noting that when depth refinement is used in combination with the depth integrity

$L_{SILog}$	$L_{inte}$	$F_{\beta}^{max} \uparrow$	$E_{\phi}^m \uparrow$	$S_{\alpha} \uparrow$	$MAE \downarrow$
		0.907	0.940	0.912	0.032
	✓	0.911	0.943	<b>0.916</b>	<b>0.030</b>
✓		0.908	0.939	0.913	0.032
✓	✓	<b>0.913</b>	<b>0.944</b>	<b>0.916</b>	<b>0.030</b>

Table 4. Ablation experiments of depth loss.

number of patches	$F_{\beta}^{max} \uparrow$	$E_{\phi}^m \uparrow$	$S_{\alpha} \uparrow$	$MAE \downarrow$	$FPS \uparrow$
$1 \times 1$	0.907	0.939	0.909	0.032	<b>7.230</b>
$2 \times 2$	0.908	0.941	0.911	0.031	7.153
$4 \times 4$	0.911	0.943	0.913	0.031	6.502
$8 \times 8$	<b>0.913</b>	<b>0.944</b>	<b>0.916</b>	<b>0.030</b>	6.043
$16 \times 16$	0.910	0.941	0.912	0.031	3.375

Table 5. Ablation of number of patches.

loss, it can increase the  $F_{\beta}^{max}$  by 0.1%, while using depth refinement alone can only increase it by 0.4%. This indicates that integrity loss can guide the network to achieve depth-guided mask prediction and makes the network tend to favor regions with smoother and more consistent depths.

#### 4.4.4 Number of Patches

To understand the impact of the number of patches during the encoder stage, we respectively set the original image to be cropped into 1, 4, 16, 64 and 256 patches as input. The calculation of FPS does not take into account the generation time of the pseudo-depth map. The results are shown in the Table 5. Contrary to MVANet [2], we found that as the number of cropped image patches increases, the performance of the model also improves till 64. There may be three reasons for this: 1: Since we only change the number of patches without changing the resolution of the image and depth, the model’s ability to extract the overall target is not weakened. 2: When the number of patches increases, the receptive field of the encoder will be limited, which may enhance the extraction of details. 3: When the number of image patches is as large as 256, the decoder’s receptive field becomes too small to reduce the detail extraction ability, because of the slight changes at the edges of window-like objects.

## 5. conclusion

In this paper, we introduce the integrity-prior through pseudo-depth maps to guide the model’s understanding of object integrity. Then, we use the fine-grained patch strategy to enhance the model’s perception of the local details of objects. We employ the Feature Selection and Extraction (FSE) to integrate depth and image patch information, and utilize the integrity-prior loss to enhance the consistency of the segmentation results in the depth map. Numerous experiments demonstrate that our model performs well on the DIS dataset. We hope that our method can contribute to the academic community’s efforts in optimizing the DIS task.



# Supplementary Material

## Patch-Depth Fusion: Dichotomous Image Segmentation via Fine-Grained Patch Strategy and Depth Integrity-Prior

### A. Integrity-Prior Loss Weight Visualization

Based on the statistical characteristics of the depth value distribution within the mask region, we aim to constrain the depth stability. We weight the loss by calculating the depth distributions of the predicted results and the target results. We use some sample results from IS-Net [1] to demonstrate how the weights change with the depth in Fig. A1.

In Fig. A1(a), the depth values within the area marked by the red frame have a large difference from the target depth values, so the weight of this area is increased. In Fig. A1(b), the depth values of the hippocampal head part within the area marked by the red frame have a small difference from the target depth values, so the weight of this part is increased.

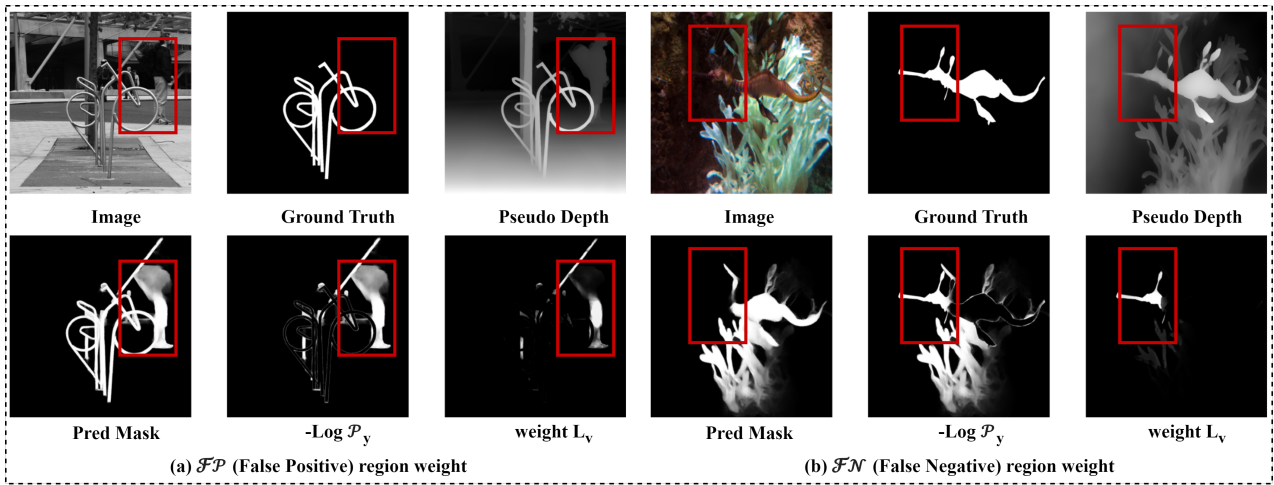


Figure A1. The weight of the integrity-prior loss varies with the changes between the predicted target and the depth map. (a) In the false negative ( $\mathcal{FN}$ ) region, the depth values are similar to the average depth of the target region, but these regions are missed in the detection. (b) In the false positive ( $\mathcal{FP}$ ) region, the depth values significantly differ from the average depth of the target region, but these regions are incorrectly detected.

### B. Qualitative ablation of Integrity-Prior Loss

We selected some samples to compare the results before and after using  $l_{inte}$  as shown in Fig. A2. It can be observed that after adding this loss term, the model has a better grasp of the depth integrity.

### C. Visualization of Depth Maps of Different Qualities

We provide more segmentation results obtained after inputting depth maps of different qualities. As shown in Fig. A3 and Table A1, depth maps of different qualities have little impact on the results.

### D. Cross-modal Attention (CoA)

Cross-modal Attention (CoA) module. Leveraging cross-attention mechanisms, CoA dynamically allocates inter-modal weights through query-key-value interactions, where complementary information is selectively enhanced via Q/K projections. The process involves: (1) Attention [24] computation  $\text{Att}(Q, K)$  between pixel sequences, (2) Integration of original Q with RMSNorm-normalized [25] attention output, (3) Non-linear enhancement through  $\text{FFN}_{\text{SwiGLU}}$  [26] with residual connections to produce final representation  $F$ . The visual architecture is shown in the Fig. A4.

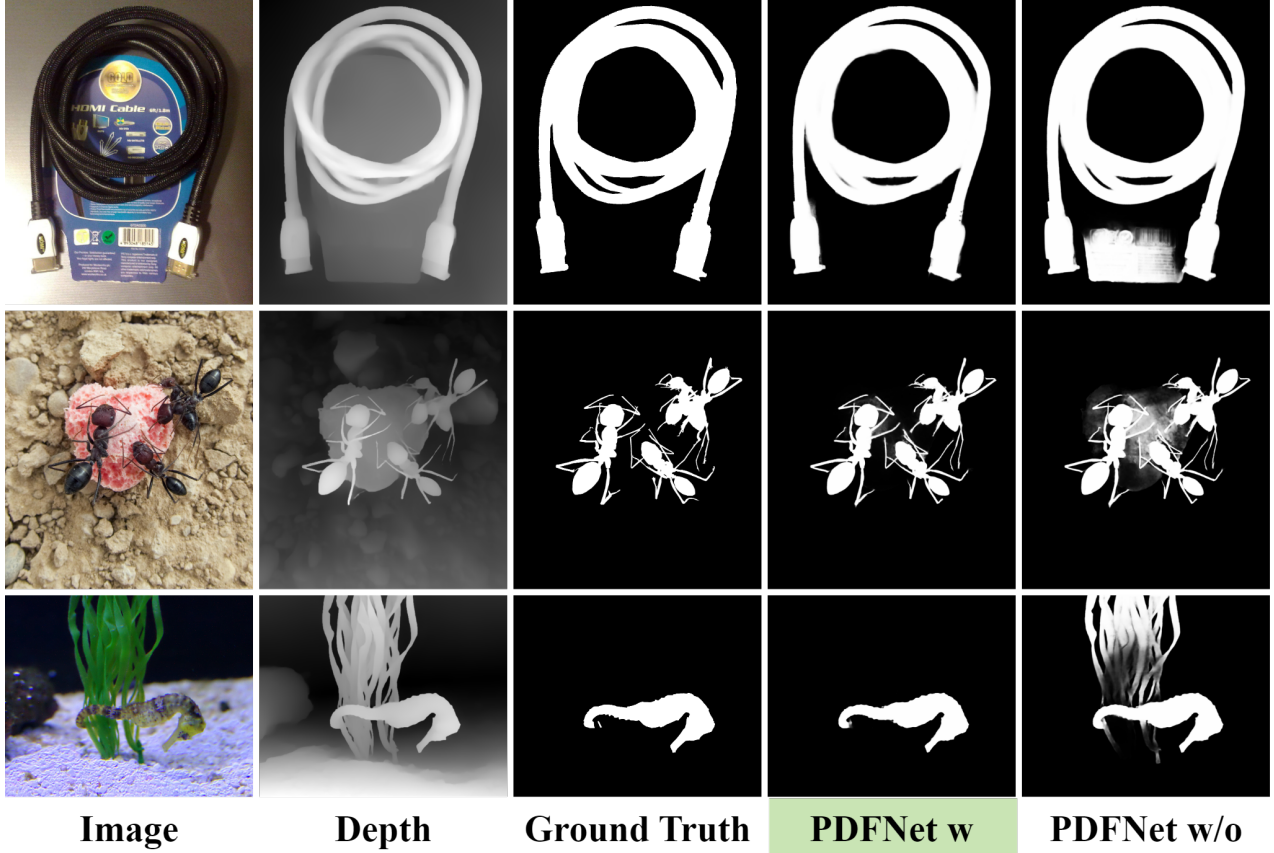


Figure A2. The comparison before and after adding  $l_{inte}$ . PDFNet with  $l_{inte}$  is referred to as PDFNet w, and PDFNet without  $l_{inte}$  is referred to as PDFNet w/o.

Depth quality	DIS-VD (470)					DIS-TE1 (500)					DIS-TE2 (500)				
	$F_{\beta}^{max} \uparrow$	$F_{\beta}^w \uparrow$	$E_{\phi}^m \uparrow$	$S_{\alpha} \uparrow$	$MAE \downarrow$	$F_{\beta}^{max} \uparrow$	$F_{\beta}^w \uparrow$	$E_{\phi}^m \uparrow$	$S_{\alpha} \uparrow$	$MAE \downarrow$	$F_{\beta}^{max} \uparrow$	$F_{\beta}^w \uparrow$	$E_{\phi}^m \uparrow$	$S_{\alpha} \uparrow$	$MAE \downarrow$
PDFNet-s	0.909	0.868	0.942	0.913	<b>0.030</b>	0.887	0.842	0.926	0.896	<b>0.031</b>	0.915	0.877	0.944	0.918	0.030
PDFNet-b	0.912	<b>0.873</b>	<b>0.944</b>	<b>0.916</b>	<b>0.030</b>	0.888	0.844	0.926	0.898	<b>0.031</b>	0.919	0.883	0.946	0.922	0.029
PDFNet-l	<b>0.913</b>	<b>0.873</b>	<b>0.944</b>	<b>0.916</b>	<b>0.030</b>	<b>0.890</b>	<b>0.846</b>	<b>0.927</b>	<b>0.899</b>	<b>0.031</b>	<b>0.921</b>	<b>0.885</b>	<b>0.947</b>	<b>0.924</b>	<b>0.028</b>
Depth quality	DIS-TE3 (500)					DIS-TE4 (500)					DIS-TE (ALL) (2,000)				
	$F_{\beta}^{max} \uparrow$	$F_{\beta}^w \uparrow$	$E_{\phi}^m \uparrow$	$S_{\alpha} \uparrow$	$MAE \downarrow$	$F_{\beta}^{max} \uparrow$	$F_{\beta}^w \uparrow$	$E_{\phi}^m \uparrow$	$S_{\alpha} \uparrow$	$MAE \downarrow$	$F_{\beta}^{max} \uparrow$	$F_{\beta}^w \uparrow$	$E_{\phi}^m \uparrow$	$S_{\alpha} \uparrow$	$MAE \downarrow$
PDFNet-s	0.932	0.893	0.955	0.924	0.028	0.906	0.860	0.938	0.906	0.039	0.910	0.868	0.941	0.911	0.032
PDFNet-b	<b>0.936</b>	0.899	<b>0.957</b>	<b>0.928</b>	<b>0.027</b>	<b>0.911</b>	0.866	0.940	<b>0.910</b>	0.038	0.914	0.873	<b>0.943</b>	0.914	<b>0.031</b>
PDFNet-l	<b>0.936</b>	<b>0.900</b>	<b>0.957</b>	<b>0.928</b>	<b>0.027</b>	<b>0.911</b>	<b>0.867</b>	<b>0.941</b>	<b>0.910</b>	<b>0.037</b>	<b>0.915</b>	<b>0.874</b>	<b>0.943</b>	<b>0.915</b>	<b>0.031</b>

Table A1. The influence of different qualities depth maps on the results during the testing.

## E. More Qualitative Evaluations

To better compare the differences between our method and other methods, we compare our PDFNet with other well-known task-related models. These models include CNN-based models such as IS-Net [1], FP-DIS [9], UDUN [10] and InSPyReNet [11], Transformer-based models like BiRefNet [12] and MVANet [2], and diffusion-based models GenPercept [13] and DiffDIS [3]. In addition, we also compare with the recent RGB-D SOD methods such as MAGNet [16] and CPNet [17], and RGB-D COD methods including DACOD [7] and RISNet [18] after they are trained on the DIS task. As shown in the Fig. A5, our method yields more accurate results for more complex scenarios, providing clearer foreground masks. Moreover, it still produces precise outputs for complex images. It can be seen that our method yields better results for transparent glass, regions with complex colors, and regions with similar colors.

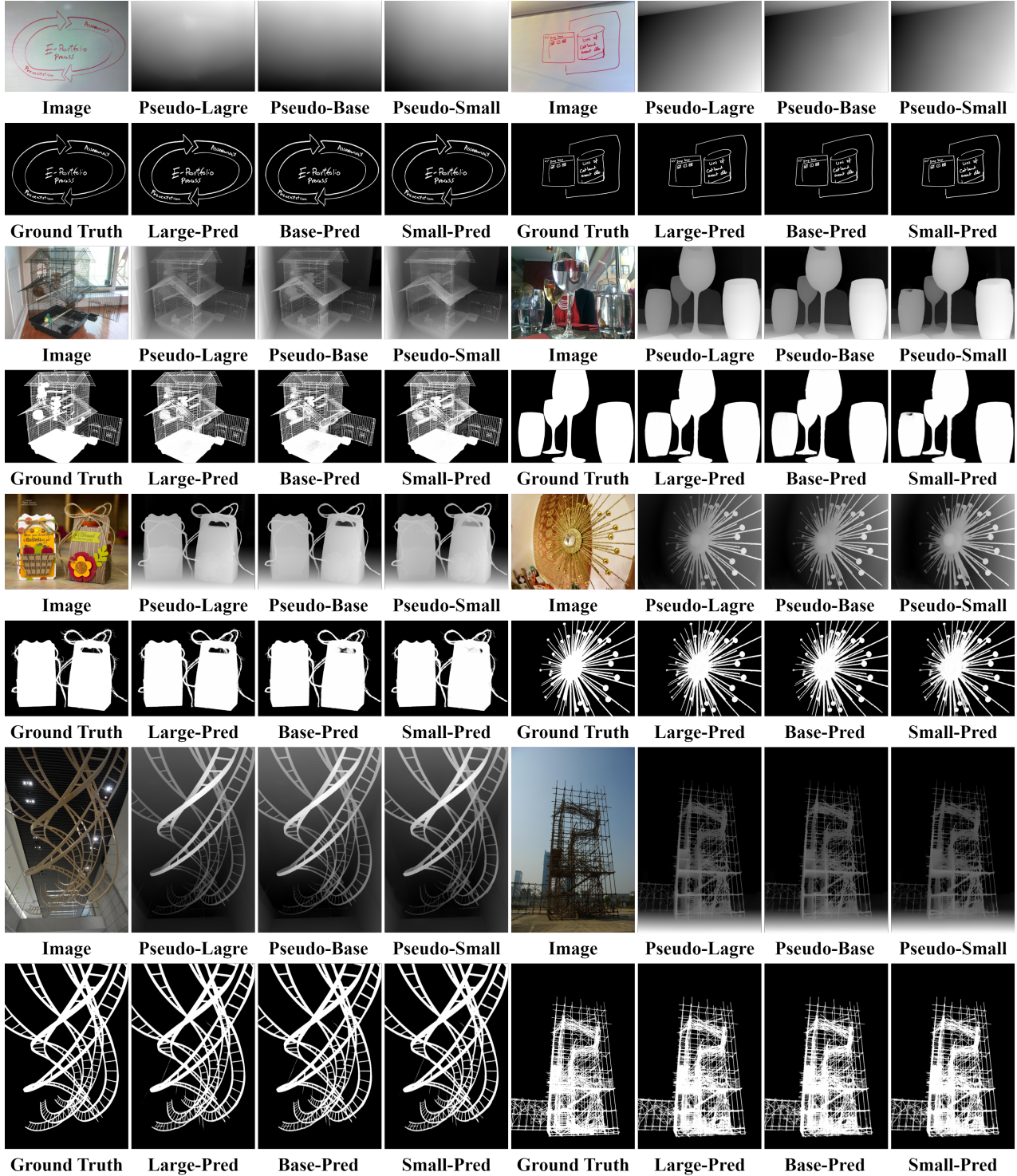


Figure A3. More qualitative results of different qualities of pseudo-depth.

## F. HRSOD Task

We conducted additional experiments on the High-Resolution Salient Object Detection (HRSOD) benchmark. Referring to [12, 41], our model was trained by combining the High-Resolution Salient Object Detection Training Set [42] (HRSOD-

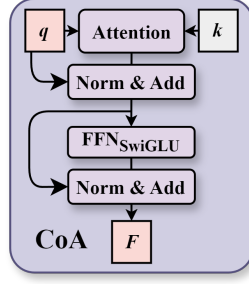


Figure A4. The architecture of CoA.

TR) (1,610 samples) and the Ultra-High-Resolution Salient Dataset Training Set [41] (UHRSD-TR) (4,936 samples), and our implementation details are consistent with those of training the DIS task, except that the number of training epochs is reduced to 40. We conducted the tests on the HRSOD-TE (400 samples) and UHRSD-TE (988 samples) with other well-known models such as PGNet [41], InSPyReNet [11] and BiRefNet [12] as shown in Table A2. We conducted some qualitative evaluation visual result as shown in Fig. A6. These results demonstrate that our method can also achieve excellent performance on other tasks.

Method	Params	HRSOD-TE (400)					UHRSD-TE (988)				
		$F_{\beta}^{max} \uparrow$	$F_{\beta}^w \uparrow$	$E_{\phi}^m \uparrow$	$S_{\alpha} \uparrow$	$MAE \downarrow$	$F_{\beta}^{max} \uparrow$	$F_{\beta}^w \uparrow$	$E_{\phi}^m \uparrow$	$S_{\alpha} \uparrow$	$MAE \downarrow$
PGNet <sub>22</sub> [41]	70M	0.939	0.901	0.960	0.938	0.020	0.939	0.917	0.955	0.935	0.026
InSPyReNet <sub>22</sub> [11]	87.5M	0.955	0.922	0.964	0.956	0.018	0.957	0.934	0.962	<b>0.953</b>	0.020
BiRefNet <sub>24</sub> [12]	215M	0.952	0.931	0.967	0.956	0.016	0.958	0.941	0.964	0.952	<b>0.019</b>
<b>PDFNet</b>	<b>94M</b>	<b>0.965</b>	<b>0.943</b>	<b>0.977</b>	<b>0.963</b>	<b>0.012</b>	<b>0.963</b>	<b>0.945</b>	<b>0.966</b>	<b>0.953</b>	<b>0.019</b>

Table A2. Performance comparisons of PDFNet with PGNet, InSPyReNet and BiRefNet.

## References

- [1] Xuebin Qin, Hang Dai, Xiaobin Hu, Deng-Ping Fan, Ling Shao, and Luc Van Gool. Highly accurate dichotomous image segmentation. In *European Conference on Computer Vision*, pages 38–56. Springer, 2022. 1, 2, 4, 6, 7, 9, 10
- [2] Qian Yu, Xiaoqi Zhao, Youwei Pang, Lihe Zhang, and Huchuan Lu. Multi-view aggregation network for dichotomous image segmentation. In *Proceedings of the IEEE/CVF Conference on Computer Vision and Pattern Recognition*, pages 3921–3930, 2024. 1, 2, 3, 4, 5, 6, 7, 8, 10
- [3] Qian Yu, Peng-Tao Jiang, Hao Zhang, Jinwei Chen, Bo Li, Lihe Zhang, and Huchuan Lu. High-precision dichotomous image segmentation via probing diffusion capacity. In *The Thirteenth International Conference on Learning Representations*, 2025. 1, 2, 6, 7, 10
- [4] Zhuoran Zheng, Chen Wu, Yeying Jin, and Xiuyi Jia. Polyp-dam: Polyp segmentation via depth anything model. *IEEE Signal Processing Letters*, 2024. 1, 3
- [5] Aleksei Bochkovskii, Amaël Delaunoy, Hugo Germain, Marcel Santos, Yichao Zhou, Stephan R. Richter, and Vladlen Koltun. Depth pro: Sharp monocular metric depth in less than a second. *arXiv*, 2024. 2, 3
- [6] Lihe Yang, Bingyi Kang, Zilong Huang, Zhen Zhao, Xiaogang Xu, Jiashi Feng, and Hengshuang Zhao. Depth anything v2. In *The Thirty-eighth Annual Conference on Neural Information Processing Systems*, 2024. 2, 3, 4, 6
- [7] Qingwei Wang, Jinyu Yang, Xiaosheng Yu, Fangyi Wang, Peng Chen, and Feng Zheng. Depth-aided camouflaged object detection. In *Proceedings of the 31st ACM International Conference on Multimedia*, pages 3297–3306, 2023. 2, 3, 6, 7, 10
- [8] Xuebin Qin, Zichen Zhang, Chenyang Huang, Masood Dehghan, Osmar R Zaiane, and Martin Jagersand. U2-net: Going deeper with nested u-structure for salient object detection. *Pattern recognition*, 106:107404, 2020. 2
- [9] Yan Zhou, Bo Dong, Yuanfeng Wu, Wentao Zhu, Geng Chen, and Yanning Zhang. Dichotomous image segmentation with frequency priors. In *IJCAI*, volume 1, page 3, 2023. 2, 6, 7, 10
- [10] Jialun Pei, Zhangjun Zhou, Yueming Jin, He Tang, and Pheng-Ann Heng. Unite-divide-unite: Joint boosting trunk and structure for high-accuracy dichotomous image segmentation. In *Proceedings of the 31st ACM International Conference on Multimedia*, pages 2139–2147, 2023. 2, 4, 6, 7, 10





Figure A5. More qualitative results of our and other methods.

- [11] Taehun Kim, Kunhee Kim, Joonyeong Lee, Dongmin Cha, Jiho Lee, and Daijin Kim. Revisiting image pyramid structure for high resolution salient object detection. In *Proceedings of the Asian Conference on Computer Vision*, pages 108–124, 2022. [2](#), [6](#), [7](#), [10](#), [12](#)
- [12] Peng Zheng, Dehong Gao, Deng-Ping Fan, Li Liu, Jorma Laaksonen, Wanli Ouyang, and Nicu Sebe. Bilateral reference for high-resolution dichotomous image segmentation. *CAAI Artificial Intelligence Research*, 3:9150038, 2024. [2](#), [4](#), [6](#), [7](#), [10](#), [11](#), [12](#)
- [13] Guangkai Xu, Yongtao Ge, Mingyu Liu, Chengxiang Fan, Kangyang Xie, Zhiyue Zhao, Hao Chen, and Chunhua Shen. What matters

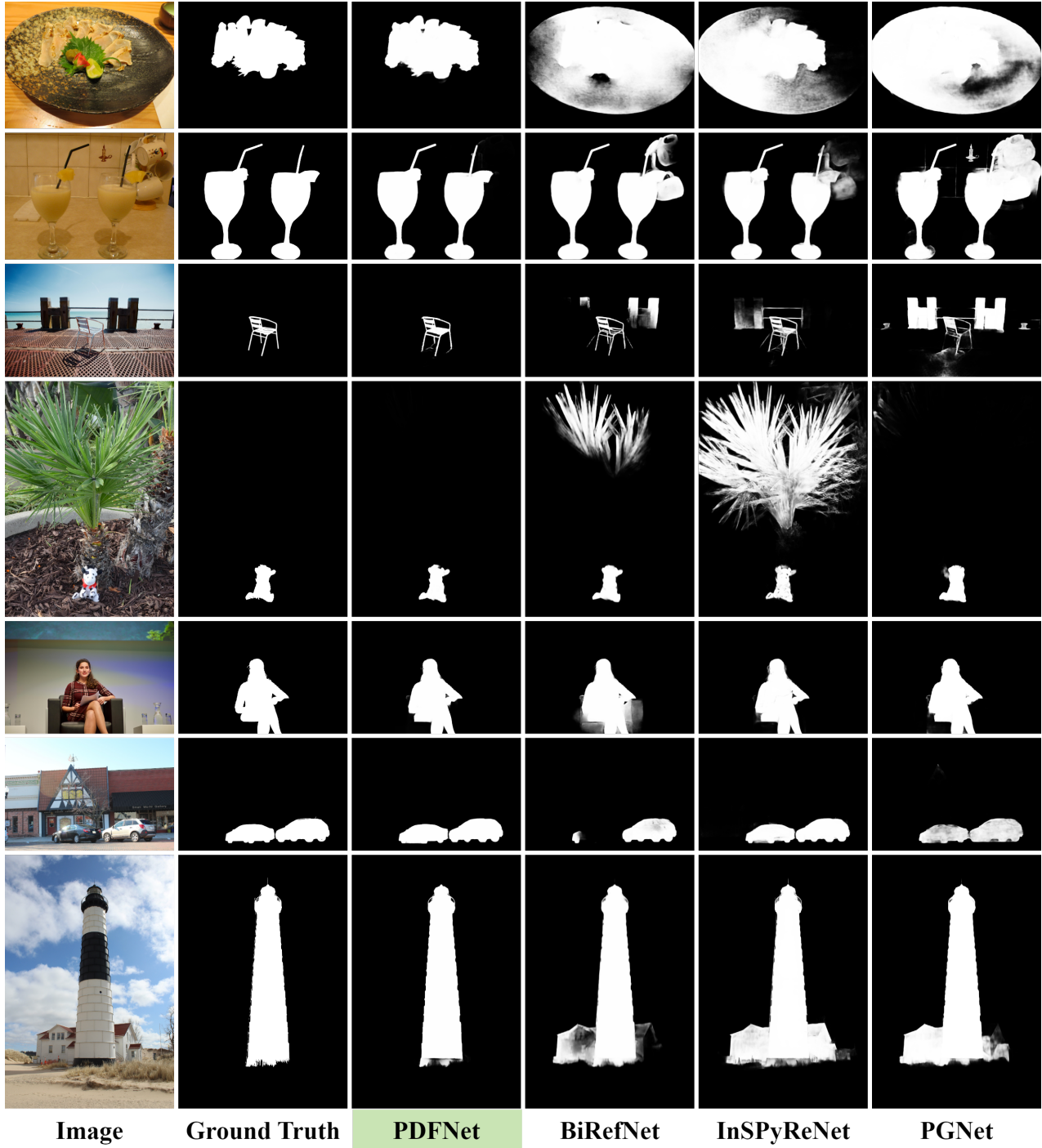


Figure A6. Some qualitative results of our and other methods about HRSOD and UHRSD.

when repurposing diffusion models for general dense perception tasks? *arXiv preprint arXiv:2403.06090*, 2024. [2](#), [6](#), [7](#), [10](#)

- [14] Clément Godard, Oisín Mac Aodha, and Gabriel J. Brostow. Unsupervised monocular depth estimation with left-right consistency. In *CVPR*, 2017. [3](#)
- [15] Lihe Yang, Bingyi Kang, Zilong Huang, Xiaogang Xu, Jiashi Feng, and Hengshuang Zhao. Depth anything: Unleashing the power of large-scale unlabeled data. In *CVPR*, 2024. [3](#)

- [16] Mingyu Zhong, Jing Sun, Peng Ren, Fasheng Wang, and Fuming Sun. Magnet: Multi-scale awareness and global fusion network for rgb-d salient object detection. *Knowledge-Based Systems*, page 112126, 2024. 3, 6, 7, 10
- [17] Xihang Hu, Fuming Sun, Jing Sun, Fasheng Wang, and Haojie Li. Cross-modal fusion and progressive decoding network for rgb-d salient object detection. *International Journal of Computer Vision*, pages 1–19, 2024. 3, 6, 7, 10
- [18] Liqiong Wang, Jinyu Yang, Yanfu Zhang, Fangyi Wang, and Feng Zheng. Depth-aware concealed crop detection in dense agricultural scenes. In *Proceedings of the IEEE/CVF Conference on Computer Vision and Pattern Recognition*, pages 17201–17211, 2024. 3, 6, 7, 10
- [19] Xinyi Yu, Ling Yan, Pengtao Jiang, Hao Chen, Bo Li, Lin Yuanbo Wu, and Linlin Ou. Boosting box-supervised instance segmentation with pseudo depth. *arXiv preprint arXiv:2403.01214*, 2024. 3, 5
- [20] Robin Schön, Katja Ludwig, and Rainer Lienhart. Impact of pseudo depth on open world object segmentation with minimal user guidance. In *Proceedings of the IEEE/CVF Conference on Computer Vision and Pattern Recognition*, pages 4809–4819, 2023. 3
- [21] Guolei Sun, Zhaochong An, Yun Liu, Ce Liu, Christos Sakaridis, Deng-Ping Fan, and Luc Van Gool. Indiscernible object counting in underwater scenes. In *Proceedings of the IEEE/CVF International Conference on Computer Vision and Pattern Recognition (CVPR)*, 2023. 3
- [22] Keren Fu, Deng-Ping Fan, Ge-Peng Ji, and Qijun Zhao. JI-dcf: Joint learning and densely-cooperative fusion framework for rgb-d salient object detection. In *IEEE Conference on Computer Vision and Pattern Recognition (CVPR)*, pages 3052–3062, 2020. 3
- [23] Jingyun Liang, Jiezhong Cao, Guolei Sun, Kai Zhang, Luc Van Gool, and Radu Timofte. Swinir: Image restoration using swin transformer. In *Proceedings of the IEEE/CVF international conference on computer vision*, pages 1833–1844, 2021. 4
- [24] A Vaswani. Attention is all you need. *Advances in Neural Information Processing Systems*, 2017. 5, 9
- [25] Biao Zhang and Rico Sennrich. Root mean square layer normalization. *Advances in Neural Information Processing Systems*, 32, 2019. 5, 9
- [26] Noam Shazeer. Glu variants improve transformer. *arXiv preprint arXiv:2002.05202*, 2020. 5, 9
- [27] Yu-Huan Wu, Yun Liu, Xin Zhan, and Ming-Ming Cheng. P2t: Pyramid pooling transformer for scene understanding. *IEEE transactions on pattern analysis and machine intelligence*, 45(11):12760–12771, 2022. 5
- [28] Zhen Zhu, Mengde Xu, Song Bai, Tengting Huang, and Xiang Bai. Asymmetric non-local neural networks for semantic segmentation. In *Proceedings of the IEEE/CVF international conference on computer vision*, pages 593–602, 2019. 5
- [29] Jun Wei, Shuhui Wang, and Qingming Huang. F<sup>3</sup>net: fusion, feedback and focus for salient object detection. In *Proceedings of the AAAI conference on artificial intelligence*, volume 34, pages 12321–12328, 2020. 6
- [30] Zhou Wang, Alan C Bovik, Hamid R Sheikh, and Eero P Simoncelli. Image quality assessment: from error visibility to structural similarity. *IEEE transactions on image processing*, 13(4):600–612, 2004. 6
- [31] René Ranftl, Katrin Lasinger, David Hafner, Konrad Schindler, and Vladlen Koltun. Towards robust monocular depth estimation: Mixing datasets for zero-shot cross-dataset transfer. *IEEE transactions on pattern analysis and machine intelligence*, 44(3):1623–1637, 2020. 6
- [32] Radhakrishna Achanta, Sheila Hemami, Francisco Estrada, and Sabine Susstrunk. Frequency-tuned salient region detection. In *2009 IEEE conference on computer vision and pattern recognition*, pages 1597–1604. IEEE, 2009. 7
- [33] Ran Margolin, Lihi Zelnik-Manor, and Ayellet Tal. How to evaluate foreground maps? In *Proceedings of the IEEE conference on computer vision and pattern recognition*, pages 248–255, 2014. 7
- [34] Deng-Ping Fan, Ming-Ming Cheng, Yun Liu, Tao Li, and Ali Borji. Structure-measure: A new way to evaluate foreground maps. In *Proceedings of the IEEE international conference on computer vision*, pages 4548–4557, 2017. 7
- [35] Deng-Ping Fan, Cheng Gong, Yang Cao, Bo Ren, Ming-Ming Cheng, and Ali Borji. Enhanced-alignment measure for binary foreground map evaluation. In *Proceedings of the 27th International Joint Conference on Artificial Intelligence*, pages 698–704, 2018. 7
- [36] Deng-Ping Fan, Ge-Peng Ji, Xuebin Qin, and Ming-Ming Cheng. Cognitive vision inspired object segmentation metric and loss function. *Scientia Sinica Informationis*, 6(6), 2021. 7
- [37] Federico Perazzi, Philipp Krähenbühl, Yael Pritch, and Alexander Hornung. Saliency filters: Contrast based filtering for salient region detection. In *2012 IEEE conference on computer vision and pattern recognition*, pages 733–740. IEEE, 2012. 7
- [38] Ze Liu, Yutong Lin, Yue Cao, Han Hu, Yixuan Wei, Zheng Zhang, Stephen Lin, and Baining Guo. Swin transformer: Hierarchical vision transformer using shifted windows. In *Proceedings of the IEEE/CVF International Conference on Computer Vision (ICCV)*, 2021. 7
- [39] Jia Deng, Wei Dong, Richard Socher, Li-Jia Li, Kai Li, and Li Fei-Fei. Imagenet: A large-scale hierarchical image database. In *2009 IEEE conference on computer vision and pattern recognition*, pages 248–255. Ieee, 2009. 7

- [40] Stefan Elfving, Eiji Uchibe, and Kenji Doya. Sigmoid-weighted linear units for neural network function approximation in reinforcement learning. *Neural networks*, 107:3–11, 2018. 8
- [41] Chenxi Xie, Changqun Xia, Mingcan Ma, Zhirui Zhao, Xiaowu Chen, and Jia Li. Pyramid grafting network for one-stage high resolution saliency detection. In *Proceedings of the IEEE/CVF conference on computer vision and pattern recognition*, pages 11717–11726, 2022. 11, 12
- [42] Yi Zeng, Pingping Zhang, Jianming Zhang, Zhe Lin, and Huchuan Lu. Towards high-resolution salient object detection. In *IEEE International Conference on Computer Vision (ICCV)*, October 2019. 11